



# Comparison of cartilage and bone morphological models of the ankle joint derived from different medical imaging technologies

Gilda Durastanti<sup>1</sup>, Alberto Leardini<sup>1</sup>, Sorin Siegler<sup>2</sup>, Stefano Durante<sup>3</sup>, Alberto Bazzocchi<sup>4</sup>, Claudio Belvedere<sup>1</sup>

<sup>1</sup>Movement Analysis Laboratory, IRCCS Istituto Ortopedico Rizzoli, Bologna, Italy; <sup>2</sup>Department of Mechanical Engineering and Mechanics, Drexel University, Philadelphia, PA, USA; <sup>3</sup>Nursing, Technical and Rehabilitation Assistance Service, IRCCS Istituto Ortopedico Rizzoli, Bologna, Italy;

<sup>4</sup>Diagnostic and Interventional Radiology, IRCCS Istituto Ortopedico Rizzoli, Bologna, Italy

*Correspondence to:* Claudio Belvedere, PhD. Movement Analysis Laboratory, IRCCS Istituto Ortopedico Rizzoli, Via di Barbiano 1/10, Bologna, Italy. Email: belvedere@ior.it.

**Background:** Accurate geometrical models of bones and cartilage are necessary in biomechanical modelling of human joints, and in planning and designing of joint replacements. Image-based subject-specific model development requires image segmentation, spatial filtering and 3-dimensional rendering. This is usually based on computed tomography (CT) for bone models, on magnetic resonance imaging (MRI) for cartilage models. This process has been reported extensively in the past, but no studies have ever compared the accuracy and quality of these models when obtained also by merging different imaging modalities. The scope of the present work is to provide this comparative analysis in order to identify optimal imaging modality and registration techniques for producing 3-dimensional bone and cartilage models of the ankle joint.

**Methods:** One cadaveric leg was instrumented with multimodal markers and scanned using five different imaging modalities: a standard, a dual-energy and a cone-beam CT (CBCT) device, and a 1.5 and 3.0 Tesla MRI devices. Bone, cartilage, and combined bone and cartilage models were produced from each of these imaging modalities, and registered in space according to matching model surfaces or to corresponding marker centres. To assess the quality in overall model reconstruction, distance map analyses were performed and the difference between model surfaces obtained from the different imaging modalities and registration techniques was measured.

**Results:** The registration between models worked better with model surface matching than corresponding marker positions, particularly with MRI. The best bone models were obtained with the CBCT. Models with cartilage were defined better with the 3.0 Tesla than the 1.5 Tesla. For the combined bone and cartilage models, the colour maps and the numerical results from distance map analysis (DMA) showed that the smallest distances and the largest homogeneity were obtained from the CBCT and the 3.0 T MRI via model surface registration.

**Conclusions:** These observations are important in producing accurate bone and cartilage models from medical imaging and relevant for applications such as designing of custom-made ankle replacements or, more in general, of implants for total as well as focal joint replacements.

**Keywords:** Human joints; computed tomography (CT); cone-beam CT (CBCT); magnetic resonance imaging (MRI); spatial registration; 3D models

Submitted Feb 06, 2019. Accepted for publication Aug 06, 2019.

doi: 10.21037/qims.2019.08.08

View this article at: <http://dx.doi.org/10.21037/qims.2019.08.08>

## Introduction

End-stage ankle osteoarthritis requires either arthrodesis or arthroplasty (1). Because of the lost joint mobility and the complications associated to bone fusion, total ankle replacement is becoming a popular alternative (2). The goal is to restore physiological joint motion, possibly ensuring natural relationships between the geometry of the articular surfaces and the tension of the ligaments (3). However, despite the recent improvements in the understanding of ankle joint biomechanics and in orthopaedic implant technology (4,5), high relevant complication and failure rates continue to afflict ankle prostheses (6-8), unlike total hip and knee replacements. The complex bone morphology, the three-planar joint kinematics, and the small dimensions, are likely to be the major contributing factors to the low survival rates (2). In addition, the small indication has contributed to both limited designs and small number of sizes available. The latter results frequently in mismatch between the geometry of the prosthesis components and the corresponding host bones.

Custom-made total ankle replacement is nowadays a viable alternative with great potentials, not only for the advantage of a personalized design of the prosthesis components, but also for their tailored dimensions, thus overcoming the issues associated to the few standard sizes currently available. Nevertheless, for this purpose, it is fundamental to provide accurate 3D models, representing very carefully the detailed three-dimensional (3D) morphology of the ankle joint (9-12) to be replaced. A customized approach based on medical imaging could definitely improve the diagnosis, the pre-surgical planning, and eventually the clinical outcomes (13-17). This is expected to lead to a better accuracy in 3D bone modelling and therefore prosthesis design, because of a thorough representation of the patient-specific bone and joint morphology. Particularly, within high-resolution medical imaging technologies, such as computed tomography (CT) and magnetic resonance imaging (MRI), identification of anatomical structures are achieved (13,18-21), traditionally for bone segments and soft tissues including the cartilage, respectively.

In addition, the recent cone-beam CT (CBCT) technology, originally for the field of dentomaxillofacial radiology (15,22-24), has proved to be also suitable to musculoskeletal radiology for upper and lower limb joints, and features reduced radiation dose, high surface and model accuracy (25,26), but mainly weight-bearing condition for

the patient during scanning. These devices finally allow to study bone and joint architecture of the extremities under physiological load (14,27-30). Because of the limited field of view (FOV), the CBCT is thus suitable for joints of small dimension (27).

Despite these new prosthesis design techniques and medical imaging technologies, the relevant literature on customized ankle prosthesis based on modern medical imaging is poor. Several studies have compared different imaging technologies, in particular CT and MRI devices, for 3D bone and cartilage model reconstructions (23,25,31,32) and for improving standard diagnosis (33,34), but mainly for the jawbone, only a few on the long bones and very few by looking at modern CBCT devices.

A number of papers have claimed comparable accuracy of MRI-based bone models with respect to CT-based models (20,35-40), though some of these studies were for other joints, but the gold standard for bone and cartilage models reconstruction remains respectively CT and MRI imaging. To take advantage of this complementary information, merging techniques between these two different imaging technologies are being exploited (35,41). In particular multimodal, i.e., between CT and MRI, registrations have been performed to achieve more effective visualization and identification of these relevant anatomical structures, also to detect pathological defects, potentially resulting in an earlier diagnosis and better treatment plan (42-44); however, this is usually performed only on 2D images. In CBCT this is achieved also with 3D representations and measurements, but this has been shown only for maxillofacial joints (43,45). The use of multimodal registration can be very beneficial in orthopaedics, especially for the ankle joints, because the morphology of the intra-articular cartilage from MRI can add value to the reconstruction of relevant bones from CT. The diagnostic performance and image quality of MRI has been enhanced considerably from the standard 1.5 Tesla to the current 3.0 and even 7.0 Tesla, which are now able to detect the cartilage layer between the bones of the joint (46,47), though not to distinguish between distal tibia and proximal talus articular cartilage. However, an accurate identification of the cartilage surface geometry, even in a single undistinguished model in between the tibial and talus, can definitely improve the patient-specific evaluation of the joint condition, and thus ensure a more correct design and planning of a joint replacement.

The purpose of the present study is to define and analyse 3D anatomical models of the tibiotalar joint derived from five CT and MRI devices and to combine these in bone

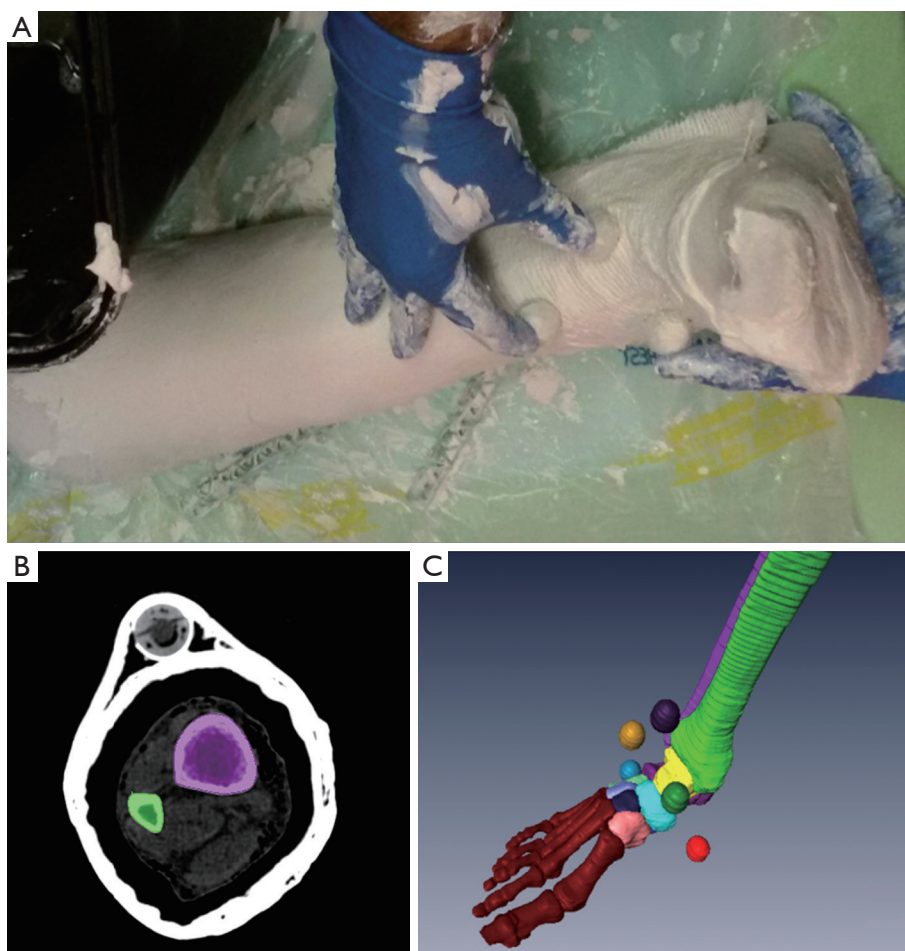


**Figure 1** Pictures from 3D bone model generation process: the specimen preparation (A), with spherical multi-modality markers stuck into the cast; and the segmentation editor (B) and final CAD models (C) from Amira software.

and cartilage models. In a single specimen, these imaging modalities were all used, and relevant spatial registrations were performed with an original procedure, to obtain models of the two bones and of the single articular cartilage in between. Validation tests were performed to assess the accuracy of geometrical reconstructions, of the bones and of the overall joint including the cartilage, through the distance map analysis (DMA) (48). The final scope is to characterise these diagnostic devices and the registrations procedures in the perspective of subject-specific modelling and custom-made prosthesis design.

## Methods

### *Specimen preparation*

A full shank and foot specimen from one male cadaver

(age 53) was analyzed. Radiographic images excluded ankle deformities, osteoarticular pathologies and cartilage defects. To maintain a rigid ankle neutral position during image scanning over the different devices, the specimen was immobilized by joint plastering. To enable registration of the models between the different devices, six multimodal imaging fiducial markers were included in the plaster. These were plastic spherical beads, 2 cm in diameter, with a spherical cavity filled with hydrogenated material and hermetically closed (*Figure 1A*).

### *Images acquisition*

For ankle models comparison, the same specimen was scanned by five different imaging devices: a standard CT (STCT) (Brilliance CT 16-slice system, Philips Healthcare),

**Table 1** Details for scans on the five medical imaging devices

Variable	CT			MRI	
	STCT	DECT	CBCT	MRI 1.5 T	MRI 3 T
Energy level	120 KVp	40 KeV	60 KVp		
Overlapping	No	No	No		
Filter	Tissue	Tissue	HD		
Sequence				Sagittal 3D cube	Sagittal 3D cube
n of excitations (NEX)				0.5	1
Eco train				80	60
Coil				Quad knee	16-ch gem flex medium
Repetition time (TR) (ms)				2.5	1.5
Echo time (TE) (ms)				8.0	3.0
Flip angle				Variable	Variable
Receive bandwidth (kHz)				62.0	83.3
Zero fill interpolation (ZIP)				512	No
Slice thickness (mm)	0.8	0.6	0.26	0.8	0.8
Slice spacing (mm)	0.8	0.6	0.26	0	0
Scan field of view (FOV) (mm)	150	150	230	200	200
Voxel size (mm)	0.29×0.29×0.8	0.29×0.29×0.6	0.26 Isotropic	0.69×0.69×0.8	0.63×0.63×0.8
Matrix	512×512	512×512	884×884	288×288	320×320

CT, computed tomography; MRI, magnetic resonance imaging; STCT, standard CT; DECT, dual energy CT; CBCT, cone-beam CT.

a dual energy CT (DECT) (Revolution HD 1700 GSI, GE), a CBCT (OnSight Extremity System, Carestream, Rochester, NY, USA), a 1.5 Tesla MRI (MRI 1.5 T; SIGNA EXCITE HDxt, GE), and a 3.0 Tesla MRI (MRI 3 T; 3T MR750W GEM ENAB, GE). Details of the imaging scans, including the coils used with both MRI, are provided in *Table 1*. These resolutions were chosen according to the overall intended context, i.e., clinical assessments of ankle arthritis and replacements.

The DECT technology allows to differentiate and quantify material composition, because of its principle that the attenuation of tissues depends on the Compton scattering and on photoelectric effects, thus on their density, anatomic number  $Z$  and also on the photon energy (49,50). The technique is performed through the simultaneous acquisition of data sets using a combination of two different X-ray spectra, generated by switching the voltage of one X-ray tube or by running two tubes at different voltages, in particular using filters of 80 and 140 kVp (50,51). The diagnostic performance of the DECT overcomes the

capabilities of conventional CT, with even reduced radiation dose (51). In agreement with radiologists and surgeons, the lowest energy level scan (40 KeV) proved to be the one that allows a better visualization and analysis of bone structures and surfaces, and therefore was chosen for this study. In perspective, this low level of energy guarantees a better protection for the patient.

The novel CBCT scanner was also used. This imaging device is characterized by a conical X-ray beam, contrasting with the fan-beam of the traditional CT; thus, the lower radiation dose results from a single rotation of the gantry required for the data acquisition of whole scan volume, incorporating the entire FOV. Sophisticated algorithms generate a volumetric data set, which can be used for the visualization of structures in all three orthogonal planes, providing 3D information. Due to isotropic voxels resolution, equal in all dimensions (15), this device can produce submillimetre resolution ranging from 0.52 to 0.26 mm; in the present study this parameter was set to 0.52 mm. Because of the smaller FOV, only the distal third

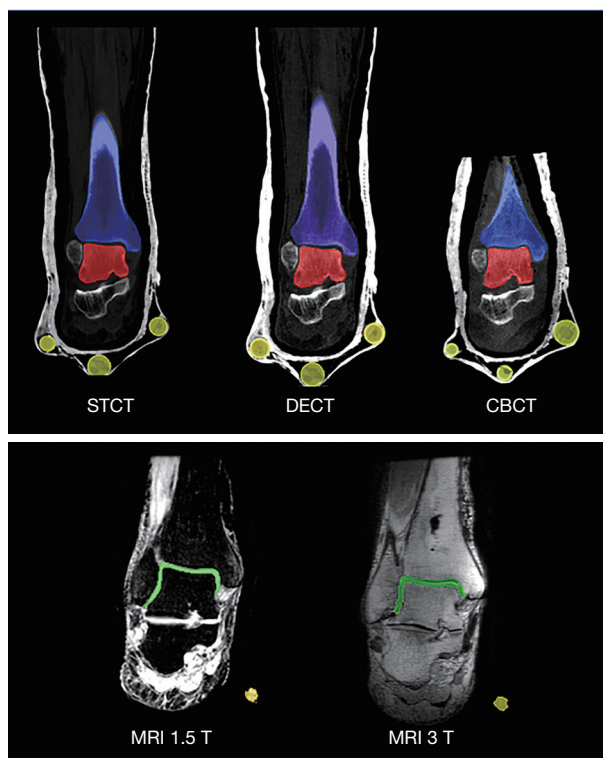


**Figure 2** Exemplary cross-sectional images from the five medical imaging devices during segmentation: bones (in red and blue) are identified from CT images, cartilage (in green) from MRI images, and markers (yellow) from both. CT, computed tomography; MRI, magnetic resonance imaging.

of the tibia was obtained.

The leg was then scanned via the two MRI devices, both with 0.3 mm spatial resolution. Among the number of collected sequences, the ‘Coronal cartil new 3D’ was taken for the MRI 1.5 T, and the ‘Sagittal PD cube’ for the MRI 3 T, because of relevant best visualization algorithms for the cartilage.

#### **Image processing: image segmentation and geometrical modelling**

All data from CT and MRI scans were exported in Digital Imaging and Communications in Medicine (DICOM) files and imported into an image visualization and processing software, Amira (Zuse Institute Berlin ZIB, Dahlem, Berlin, Germany - Thermo Fisher Scientific, Waltham, MA, USA), to obtain 3D models by a manual/semi-automatic segmentation (Figure 1B) and reconstruction algorithms (Figure 1C) (52,53); 2D segmented images were combined

to produce representation of the external surface of the two bones and of a single tibiotalar articular cartilage, as well as of the spheres of the multimodal markers.

The manual segmentation process is time-consuming and error-prone, but it guarantees a proper and accurate identification of the boundaries of these structures (54). In particular, a number of different tools were used; among these, when thresholding was exploited, the Hounsfield unit values were set slice by slice, according to the quality of the image to be segmented: for most of these, this was in the range 300–900. Tibia, talus and marker segments were reconstructed separately from the three CT devices; single tibiotalar cartilage and marker segments from the two MRI devices (Figure 2). These 3D models were then exported from Amira as stereolithography (STL) files, and imported for smoothing and minor spike adjustments in a computer-aided design software, Geomagic Studio (3D Systems, Rock Hill, USA). For the ‘smoothness’, ‘strength’ and ‘curvature priority’ parameters, all with range from 1 to 8, the values set were respectively 6, 6 and 8. The calculation of the centre of the best-fit sphere for every marker and all the following analyses were then performed in Geomagic Control.

This segmentation and model reconstruction procedure was all performed by a single expert operator, and repeated by the same operator a few weeks later.

#### **Registration of 3D models**

To compare models from the different medical imaging technologies, and also to obtain complete bone plus cartilage models of the entire ankle joint, the registration bone-to-bone from CT models, cartilage-to-cartilage from MRI models, and combined cartilage-to-bone from all MRI- and CT-based models were performed (44).

The following two registration methods were used. The singular value decomposition (SVD) algorithm (55) is a spatial registration between two 3D models guided by a limited number of well-defined common points, and was performed by the ‘RPS Alignment’ tool in Geomagic Control (Figure 3A). The calculated centres of the six multimodal markers were taken as these corresponding points. The quality of this registration is here provided by the deviation values for every pair of the points.

The iterative closest point (ICP) algorithm (56) was also used; it is a best-fit alignment of two objects based on the spatial matching of all their points (Figure 3B), and was implemented as a Geomagic Control. A least-squares

method is employed, where the sums of squares of distances between sampled pairs are minimized over all the rigid motions between the objects. The closest points are then established and a relevant transformation matrix is provided. In other words, this best-fit registration consists of surface overlapping in the optimal positioning of the objects to minimize registration errors in terms of mean distance of the two corresponding surfaces. Because of the smaller model of the tibia associated to the FOV of the CBCT, the other two corresponding CT-based models were shortened accordingly.

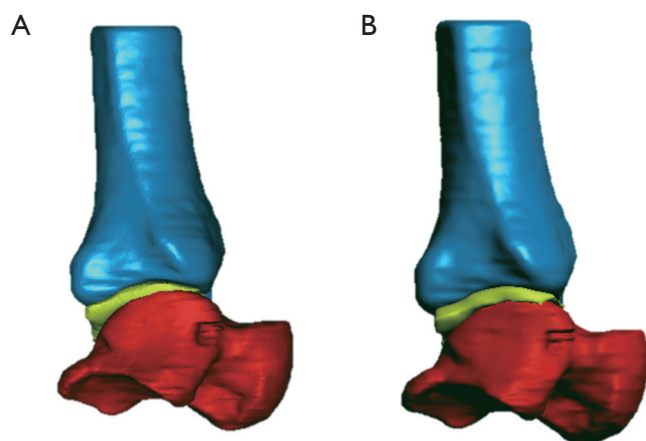


**Figure 3** Exemplary results of multi-modal model registration, via SVD (A) and via ICP (B). The bone models of the talus (in red) and tibia (in blue) are depicted together with the model (in lemon-green) of the single tibiotalar articular cartilage. SVD, singular value decomposition; ICP, iterative closest point.

In all cases, the result is a best possible superimposition of the corresponding models, proving the magnitude of deviation between the surfaces of the two registered volume objects: the error values of the overall spatial registration, i.e., the mean error and the root mean square (RMS), which is used as an absolute measure of model surface deviations.

### DMA

To assess the quality of these single and combined models also after these registration procedures, DMA was used as surface-to-surface analysis, performed by ‘3D compare’ tool in Geomagic Control (48,57). In this tool, the ‘3D deviation’ type was set, for which the shortest distance from each point on one surface (the ‘Test’) to any point on the other (the ‘Reference’) is reported as the result. A corresponding colour-coded map is also generated as a graphic representation of these 3D distances between the two surfaces with a gradient of colours on the reference object. In addition, the ‘critical angle’ and the ‘maximum deviation’ parameters were set respectively at 180° at 6 mm. The distance map provides the following statistical values: maximum distance, mean positive and mean negative distances, standard deviation (SD) and RMS. This analysis was performed between any pair of bone models out of the three different CT-based (Figure 4) for both talus and tibia, and between the six models which combined after spatial registration the three CT-based bone models and the two MRI-based cartilage models (Figure 5).

By definition, differences are marked positive and negative when the tested surface lies respectively outside

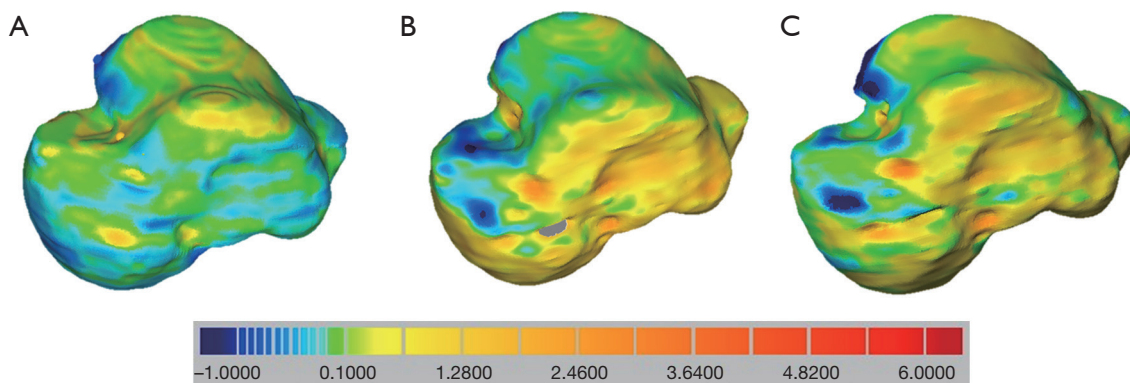


**Figure 4** Results from the distance map analysis, after bone-to-bone registration via SVD: STCT-DECT (A); DECT-CBCT (B); STCT-CBCT (C). Colour-map is from maximum penetration (–1 mm, in blue) to maximum separation (6 mm, in red) passing for a best matching (in green), as for the colour scale. SVD, singular value decomposition; STCT, standard CT; DECT, dual energy CT; CBCT, cone-beam CT; CT, computed tomography.

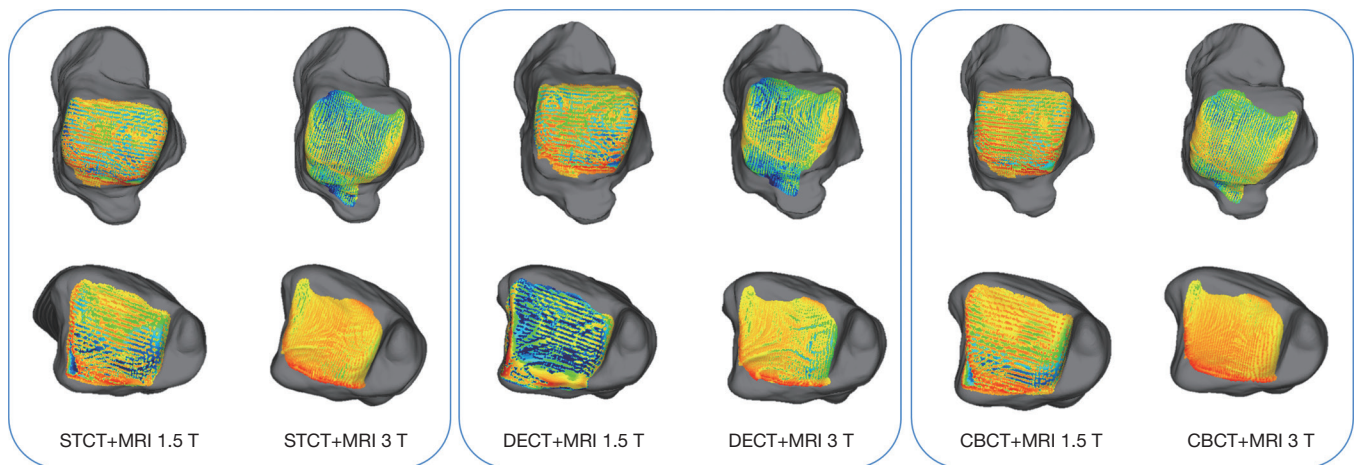


**Figure 5** Results from DMA for each combination of cartilage-to-bone models, all obtained through ICP registration: for both the talus (top row) and the tibia (bottom), the diagrams show the map of the distance between the model of the bone and the model of the individual cartilage. Bone models were from STCT (left), DECT (central), and CBCT (right); each combined with both cartilage models, i.e., from MRI 1.5 T and MRI 3 T. DMA, distance map analysis; ICP, iterative closest point; STCT, standard CT; DECT, dual energy CT; CBCT, cone-beam CT; CT, computed tomography; MRI, magnetic resonance imaging.

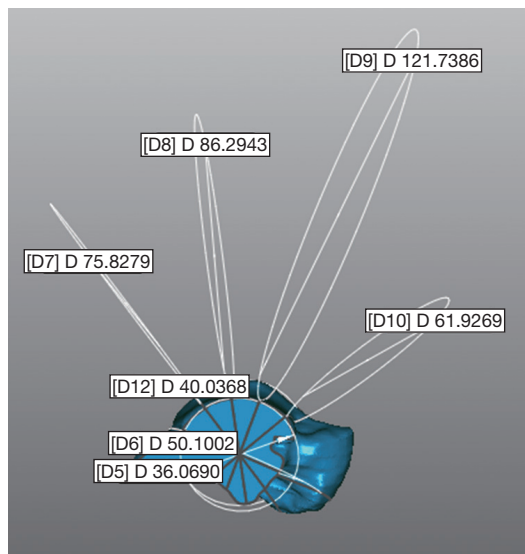


**Figure 6** Snapshot depicting how the 3D geometrical parameters are extrapolated on the talus model (here the one obtained from the CBCT scan). CBCT, cone-beam CT; CT, computed tomography.

and inside the reference surface. In all these colour maps, the perfect matching between the two objects is represented by green, yellow/red areas represent progressive positive distances, i.e., separation, whereas the dark-/light- blue areas represent progressive negative distances, i.e.,

penetration, of the surfaces.

#### *Calculation of talar geometrical parameters*

In the perspective of exploitations in ankle replacements, the effect of the quality of the bone models on the calculated parameters for a possible personalized prosthesis design was also investigated (Figure 6).

According to a recent original procedure from experimental and modelling analyses of ankle morphology (11), the talus trochlear surface was approximated to an original saddle-shaped, skewed, truncated cone with apex on the lateral side, in contrast to pioneering studies (58,59). This procedure, performed in Geomagic Control, determines seven circles best fitting the following: the medial and lateral crest of the trochlea tali, and five equidistant arcs along the trochlear groove, from the most anterior to the most posterior (Figure 6). This was performed in each of the three talus models from CT scans.

#### *Validation*

To assess the technical reliability of the entire procedure as here above, the quality of the marker spherical models from CT scans was analysed. A corresponding 2 cm diameter numerical spherical model was defined, and this registered to each of these six multimodal markers. For each of these

**Table 2** Statistical values of DMA between reconstructed markers and the corresponding numerical model

Variable	Standard CT	Dual energy CT	Cone-beam CT
Max deviation (+)	1.57±0.30	1.98±0.61	1.18±0.32
Max deviation (-)	-0.39±0.17	-0.44±0.22	-0.47±0.27
Mean (+)	0.62±0.11	0.78±0.20	0.39±0.08
Mean (-)	-0.12±0.05	-0.14±0.06	-0.11±0.07
SD	0.37±0.09	0.59±0.22	0.36±0.18
RMS	0.68±0.13	0.88±0.21	0.46±0.11

Values (mean ± standard deviation over the six markers) are all in millimetres. CT, computed tomography; DMA, distance map analysis; SD, standard deviation; RMS, root mean square.

**Table 3** Number of triangles for all the models, developed from segmentation of CT and MRI scans and analyzed

Variable	STCT	DECT	CBCT	MRI 1.5 T	MRI 3 T
Talus	89,574	153,222	85,580	24,862	106,888
Tibia	388,558/106,352	235,426/173,644	104,566	37,072	157,320
Cartilage	-	-	-	8,874	29,161

For the tibia, STCT and DECT values show the full/half size, the latter for a comparison with the CBCT. STCT, standard CT; DECT, dual energy CT; CBCT, cone-beam CT; CT, computed tomography; MRI, magnetic resonance imaging.

registrations, the DMA was performed.

## Results

### Validation

DMA of this overall procedure, measured by fiduciary marker matching, showed small values (*Table 2*), revealing a good quality of the entire process of imaging, segmentation, 3D reconstruction and spatial registration. These values are also consistent over the three CT devices, with the best 3D reconstruction of the marker models from the CBCT device (mean RMS 0.46).

### Registration of 3D models, and DMA

The resolution of the two bones and the single cartilage models obtained from all the CT and MRI scans is shown in *Table 3*. Very good results from DMA were obtained from all the bone-to-bone model registrations from CT devices with both the SVD and ICP registration procedures (*Table 4*). The RMS of the ICP registration for the tibia was a bit larger than that for the talus (*Table 4*), likely due to the slight differences in length among the bone models from the three devices. RMS from the DMA were also found smaller than

1 mm, and only small differences were observed among the three devices, and between the bones and the registration techniques.

When the same was performed between bone models from MRI the results were very unsatisfactory: because of the multimodal markers with the SVD registration procedure, and likely because of the quality of the MRI-based bone models with the ICP procedure. When the bone models from the three CT devices were registered to those from the two MRI devices, the bone-to-bone mean registration error over the six combinations were in the range of 0.7–1.0 mm for the talus, and 0.7–1.1 mm for the tibia, much larger than the corresponding between the three CT-based bone model combinations (*Table 4*). When the two MRI-based bone models were registered to each other, this mean error was 0.8 mm for the talus and 1.8 for the tibia.

As for the comparison of the two cartilage models, i.e., from MRI 1.5 T and MRI 3 T, both the cartilage-to-cartilage ICP and the marker-based SVD registrations resulted in RMS values about 3 and 6 times larger respectively than those observed between CT models, likely due to the very different resolution between the two MRI devices.

**Table 4** Results from the registration process and DMA, for the two bones, and for both the SVD and ICP registration technique

Variable	Registration		Distance map analysis		
	Mean error	RMS	Max distance (+)	Max distance (-)	RMS
SVD					
Talus					
STCT vs. DECT	0.4	0.4	1.2	-2.0	0.5
DECT vs. CBCT	0.3	0.3	3.6	-3.3	0.7
STCT vs. CBCT	0.2	0.2	2.5	-2.5	0.5
Tibia					
STCT vs. DECT	0.4	0.4	1.1	-1.5	0.3
DECT vs. CBCT	0.3	0.3	2.6	-1.6	0.9
STCT vs. CBCT	0.2	0.2	2.5	-1.3	0.9
ICP					
Talus					
STCT vs. DECT	0.3	0.4	1.2	-2.1	0.4
DECT vs. CBCT	0.5	0.7	3.6	-3.3	0.7
STCT vs. CBCT	0.3	0.4	2.9	-2.2	0.4
Tibia					
STCT vs. DECT	0.3	0.4	1.3	-1.4	0.3
DECT vs. CBCT	0.6	0.8	2.0	-1.0	0.7
STCT vs. CBCT	1.0	1.5	1.7	-0.9	0.7

Measurements are in mm. DMA, distance map analysis; SVD, singular value decomposition; ICP, iterative closest point; STCT, standard CT; DECT, dual energy CT; CBCT, cone-beam CT; CT, computed tomography; RMS, root mean square.

The DMA results of the six combined cartilage-to-bone models, i.e., from the three CT bone models and the two MRI cartilage models, are reported in *Figure 5* and *Table 5*. Registration was obtained for the talus bone only, via ICP, with the RMS of this registration being  $0.95 \pm 0.09$  (range, min-max: 0.91–1.10) on average over all combinations; equivalent registration values via SVD resulted in about two times larger RMS distances. From these six, the DMA between the cartilage model from the two MRI scans and both the talus (top of *Table 5*; yellow and red models in *Figure 3A*) and the tibia (bottom of *Table 5*; yellow and blue in *Figure 3A*) from CT were performed; in other words, this is called matching of the chemical shift layers of the tibiotalar joint. RMS values toward the talus bone models of the cartilage model from MRI 3 T are all smaller than those from MRI 1.5 T; the same applies also for the maximum negative distance toward the tibia, i.e., penetration peaks for these models. By looking at both *Figure 5* and *Table 5*, more

homogeneity of the colour map was found for the MRI 3 T models with respect to MRI 1.5 T. *Table 5* also reveals more separation than penetration, by looking at both peak and mean distances.

#### Calculation of talar geometrical parameters

The calculated diameters of the circles best fitting the medial and lateral crests of the talus compared well among the bone models from the three CT devices (*Table 6*). These diameters also reveal the conical shape of the trochlea tali, with apex laterally. The circles over the trochlear groove were found less consistent over the models, best consistency being at the posterior-central section of the trochlea. The best circles at the most posterior section are in the plantar aspect, representing the convexity of this part of the trochlea tali.

The repeatability analysis performed on CT-based bone

**Table 5** DMA at the six combined cartilage-to-bone models, i.e., from the three CT bone models and the two MRI cartilage models; registration was obtained by the talus model via ICP. Both the surfaces of the cartilage, toward the talus (top) and toward the tibia (bottom) are reported

Variable	Max distance (+)	Max distance (-)	Mean distance	SD	RMS
Cartilage toward talus					
STCT + MRI 1.5 T	6.0	-1.2	1.7	1.8	2.5
STCT + MRI 3 T	3.6	-2.0	0.3	1.3	1.3
DECT + MRI 1.5 T	6.0	-1.2	1.7	1.8	2.5
DECT + MRI 3 T	3.6	-2.2	0.3	1.3	1.3
CBCT + MRI 1.5 T	6.0	-0.9	2.0	1.8	2.6
CBCT + MRI 3 T	4.0	-1.4	0.7	1.3	1.5
Cartilage toward tibia					
STCT + MRI 1.5 T	6.0	-1.8	1.5	1.9	2.4
STCT + MRI 3 T	6.0	-0.6	0.9	1.5	2.4
DECT + MRI 1.5 T	6.0	-4.6	0.0	2.3	2.3
DECT + MRI 3 T	6.0	-1.0	1.5	1.6	2.2
CBCT + MRI 1.5 T	6.0	-1.2	1.9	1.8	2.6
CBCT + MRI 3 T	6.0	-0.2	2.2	1.6	2.7

Measurements are in mm. DMA, distance map analysis; ICP, iterative closest point; STCT, standard CT; DECT, dual energy CT; CBCT, cone-beam CT; SD, standard deviation; RMS, root mean square; CT, computed tomography; MRI, magnetic resonance imaging.

**Table 6** Calculated diameters of the seven best fit circles, for each of the CT-based models: negative values in the last column represent the observed circles located toward the plantar aspect of the foot (see also *Figure 5*)

Variable	Crest medial	Crest lateral	Trochlea anterior	Trochlea ant.-cent.	Trochlea central	Trochlea post.-cent.	Trochlea posterior
STCT	39.5	33.8	85.3	70.7	59.4	76.2	85.2 (-)
CBCT	40.0	36.1	62.0	121.7	86.3	75.9	50.1 (-)
DECT	42.5	36.9	45.3	92.1	62.3	74.2	80.8 (-)

Measurements are in mm. STCT, standard CT; DECT, dual energy CT; CBCT, cone-beam CT; CT, computed tomography.

models showed that the intra-operator error was 0.1 mm in terms of mean error of registration, which compares very well with the values in *Table 4*. This resulted in a percentage error smaller than 7 % for the talar geometrical parameters. All concluding observations on the models' quality from the different imaging modalities and the registration techniques remained the same.

## Discussion

In this study, an in-depth morphological analysis via a multiple comparison of anatomical 3D models of the ankle joint was performed. The models included the full talus and

tibia bones, and the single tibiotalar cartilage in between: for the first time these derived from a single specimen secured in a single rigid position, and by using five different medical imaging devices, i.e., three CT and two MRI. The results in isolated bone or cartilage models, and also in complete bone plus cartilage models, showed different reliability of these devices, and are therefore of value for future exploitations particularly in subject-specific skeletal modelling and custom-made prosthesis design.

In fact, to overcome the current issues in ankle replacement, a personalized design of the prosthesis should mimic better bone and articular cartilage morphology, based on current or even novel anatomical model approximations

(11,60). Within this context, state-of-the-art medical imaging devices were assessed in the present study for their role in the creation of 3D single anatomical models, along with a best possible merging of the two bone models from CT and the single cartilage model from MRI. Though recent literature have reported studies on multimodal registration of data derived from different imaging acquisition technologies, they are generally associated to 2D modality or related to other anatomical complexes (42-44,61,62). In most of these cases, several issues regarding registration methods and related accuracy have been raised and discussed (41,45), together with the accuracy evaluation of reconstructed geometrical models obtained via CT and MRI imaging (32,35,36). As for the important issue pertaining to bone reconstruction of the whole surface geometry by separating/merging cortical and sub-chondral bone, only one study reported an original methodology to assess relevant segmentation and accuracy in model-to-model registration, though using only the ICP registration method (63). This method however, used to register CT- and MRI-based models, was demonstrated to be the most robust (41,45), as found also in the present study. In addition, a recent *in-vitro* study (32) using DMA to assess registrations of reconstructed bones only, i.e., no cartilage models were considered, reported a mean difference between models smaller than 1 mm, which is consistent with what is reported in the present study. In general, not a single paper has shown 3D morphological models including bones and cartilage, respectively from CT and MRI, nor registered these for subsequent thorough DMA as in the present study.

In the present study, an emerging medical imaging technology was also assessed, i.e., the CBCT, and compared with traditional CT-based devices. This allows high spatial resolution revealing accurate anatomical details, such as articular surfaces, even bone micro-architecture and soft tissue (64,65), fast imaging acquisition time, easy installation, low radiation dose and lower costs compared to conventional CT (22,66) and weight-bearing postures, which is a major limitation of conventional CT (29). These features represent a considerable advantage, particularly in the evaluation of osteochondral lesions of the ankle joint (27). This has been shown in CBCT scans of the lower extremities (29,67), under a number of weight-bearing conditions (14), and in many studies on bone and joint degenerative changes, at the knee, ankle and foot (14,27).

The good quality of this overall imaging, modelling and registration process was supported by RMS distances between measured and known shapes of the multimodal

markers, found to be always smaller than 1 mm (*Table 2*). The best result were found for those marker models from CBCT scans, likely accounted for to the smaller registration error with this device when the SVD registration technique was used. DMA was used also for the comparison of corresponding anatomical models, after registration in space by the two different techniques; these results did not reveal considerable differences between the two MRI and between the three CT devices (*Table 4*). These results, however, did not reveal considerable differences between the different devices of the same image modality. This overall general consistency also for the bone models, however, did not result in uniformity of the calculated talar parameters: the diameters of the circles representing the trochlea tali sections were very different between the three CT-based bone models (*Table 6*), especially for the sections with large diameters. The obtained geometrical parameters from this specimen are consistent with the representation of the trochlea tali as a truncated cone with apex on the lateral side (11).

In the present experimental and analytical exercise, the ICP registration worked better than the SVD. Because the former is based on the spatial match of general clouds of many points and the latter on a few known points, it is deduced that the 3D anatomical models from the different devices are more consistent than the corresponding marker clusters. Particularly, the visibility of these experimental multimodal markers turned out to be not very successful in the MRI scans. This better performance of ICP can be observed by looking at the registration errors, but also at the DMA (*Table 4*): the ICP registration resulted in fact in more homogeneity over the surfaces and in less overall penetration. For the combined cartilage and bone models, the colour maps (*Figures 3 and 5; Table 5*) and the numerical results from DMA show that the smallest distances and the largest homogeneity were obtained from the CBCT and MRI 3 T combination via ICP registration (*Figure 5*) and the worst from MRI 1.5 T.

This study is not free from limitations. First of all, the present series of medical imaging scans *in vitro* prevented realistic reconstruction of physiological loading conditions. In addition, the use of a single specimen and the manual segmentation procedure, though performed by a single operator, could have influenced the quality the final anatomical 3D models (57), in particular for the calculation of the talar parameters for prosthesis design. The present preliminary repeatability analysis shows that the observations are maintained also for other processing sessions of the same operator. Finally, segmentation of

the cartilage in the MRI scans was critical as expected, particularly when the boundaries are to be identified. To address this issue, the input parameters necessary for 3D reconstruction, the model registration, the talar diameter calculations and the DMA were set and maintained carefully, possibly maximising the repeatability of the measurements. Nevertheless, the articular surface geometry could not be distinguished between tibial and talar, and the final cartilage model after 3D reconstruction represented a single surface (*Figure 3*). This is a known limitation of MRI scans of human joints; the distinction of these two cartilage surfaces would require either their physical separation, or interposition of other material, which are all not feasible within the exploitation context of these techniques, i.e., patient specific ankle replacement. Although separate distinguished cartilage models may help a more careful design of these replacements, the present single surface is still a good value because eventually the remaining cartilage in between is to be removed during this surgery of arthritic ankles, and because it is the amount of bone left which influences the most the decisions on prosthesis component dimensions and locations.

Among the major overall issues in these multimodal analyses there are the registration objects and techniques. Eventually, the home-made multi-modal markers proved to be less accurate than expected in MRI. Because of the known polarisation effect of the relevant material and a small number of slices, oblong rather than spherical geometries were obtained from MRI scans, affecting considerably the results of the SVD registration. These multi-modal markers however are believed to be fundamental for 3D spatial registration between bone models from CT and cartilage models from MRI (68,69), avoiding the critical identification of common anatomical landmarks. This merging, either by SVD or ICP registration procedures, is still considered as the gold standard to obtain reconstructions of complete anatomical models of the diarthrodial joints, which can include the bones and the cartilage in between. The alternative would be defining these bones plus cartilage models from MRI scans only, but our present results show that the accuracy of the MRI-based bone models is higher than that of the gold STCT-based models, though a number of studies have claimed comparable results (20,35-40). MRI-based 3D models of the bone have shown comparable accuracy with respect to CT-based models (35-37,40,41), even in presence of normal and dysplastic anatomical structures (37). However, a number of these are not about human ankle

joints, or were for other applications. When corresponding quantitative comparisons were reported, the  $1.1 \pm 0.3$  mm global 3D contour error between MRI- and CT- based models (41), compares well with what here reported (range 0.7–1.1 mm).

## Conclusions

In conclusion, after careful morphological analyses of anatomical 3D models from different imaging modalities, the best bone and cartilage models, in terms of reconstruction and registration, were here obtained respectively with the CBCT and MRI 3 T devices. The combination of these two imaging technologies are also suggested in case of a complete bone plus cartilage models of the ankle, because of the relevant and most homogenous colour map, with less penetration and a better matching between the models. A clear exploitation of these results is in the definition of subject-specific morphological models of this joint, leading to a more accurate identification of articulating surfaces, and a careful reproduction of the natural morphology and anatomy of relevant bones and cartilage, which is necessary in radiographic assessments and skeletal modelling. These are important observations also in planning and designing ankle replacements, either for prostheses in standard sizes, custom total replacements, or even for metallic focal resurfacing implant (70).

## Acknowledgments

*Funding:* This study was support by the Italian Ministry of Economy and Finance within the program “5 per mille”, and by Regione Emilia-Romagna (Italy), program POR-FESR Project 726346-Custom-implants.

## Footnote

*Conflicts of Interest:* The authors have no conflicts of interest to declare.

## References

1. Mercer J, Penner M, Wing K, Younger AS. Inconsistency in the Reporting of Adverse Events in Total Ankle Arthroplasty: A Systematic Review of the Literature. *Foot Ankle Int* 2016;37:127-36.
2. Leardini A, O'Connor JJ, Giannini S. Biomechanics of the natural, arthritic, and replaced human ankle joint. *J Foot*

- Ankle Res 2014;7:8.
3. Leardini A, O'Connor JJ, Catani F, Giannini S. Mobility of the human ankle and the design of total ankle replacement. *Clin Orthop Relat Res* 2004;39-46.
  4. Cenni F, Leardini A, Cheli A, Catani F, Belvedere C, Romagnoli M, Giannini S. Position of the prosthesis components in total ankle replacement and the effect on motion at the replaced joint. *Int Orthop* 2012;36:571-8.
  5. Cenni F, Leardini A, Pieri M, Berti L, Belvedere C, Romagnoli M, Giannini S. Functional performance of a total ankle replacement: thorough assessment by combining gait and fluoroscopic analyses. *Clin Biomech (Bristol, Avon)* 2013;28:79-87.
  6. Spirt AA, Assal M, Hansen ST, Jr. Complications and failure after total ankle arthroplasty. *J Bone Joint Surg Am* 2004;86-A:1172-8.
  7. Yu JJ, Sheskier S. Total ankle replacement--evolution of the technology and future applications. *Bull Hosp Jt Dis (2013)* 2014;72:120-8.
  8. Vander Griend RA, Younger ASE, Buedts K, Chiodo CP, Coetzee JC, Ledoux WR, Pinzur MS, Prasad K, Queen RM, Saltzman CL, Thordarson DB. Total Ankle Arthroplasty: Minimum Follow-up Policy for Reporting Results and Guidelines for Reporting Problems and Complications Resulting in Reoperations. *Foot Ankle Int* 2017;38:703-4.
  9. Schmutz B, Rathnayaka K, Wullschlegel ME, Meek J, Schuetz MA. Quantitative fit assessment of tibial nail designs using 3D computer modelling. *Injury* 2010;41:216-9.
  10. Belvedere C, Siegler S, Ensini A, Toy J, Caravaggi P, Namani R, Giannini G, Durante S, Leardini A. Experimental evaluation of a new morphological approximation of the articular surfaces of the ankle joint. *J Biomech* 2017;53:97-104.
  11. Siegler S, Toy J, Seale D, Pedowitz D. The Clinical Biomechanics Award 2013 -- presented by the International Society of Biomechanics: new observations on the morphology of the talar dome and its relationship to ankle kinematics. *Clin Biomech (Bristol, Avon)* 2014;29:1-6.
  12. Belvedere C, Siegler S, Fortunato A, Caravaggi P, Liverani E, Durante S, Ensini A, Konow T, Leardini A. A New Comprehensive Procedure for Custom-Made Total Ankle Replacements: Medical Imaging, Joint Modeling, Prosthesis Design, and 3d Printing. *J Orthop Res* 2019;37:760-8.
  13. Gargiulo P, Helgason T, Ramon C, Jonsson H Jr, Carraro U. CT and MRI Assessment and Characterization Using Segmentation and 3D Modeling Techniques: Applications to Muscle, Bone and Brain. *Eur J Transl Myol* 2014;24:3298.
  14. Barg A, Bailey T, Richter M, de Cesar Netto C, Lintz F, Bursens A, Phisitkul P, Hanrahan CJ, Saltzman CL. Weightbearing Computed Tomography of the Foot and Ankle: Emerging Technology Topical Review. *Foot Ankle Int* 2018;39:376-86.
  15. Scarfe WC, Li Z, Aboelmaaty W, Scott SA, Farman AG. Maxillofacial cone beam computed tomography: essence, elements and steps to interpretation. *Aust Dent J* 2012;57 Suppl 1:46-60.
  16. Fokas G, Vaughn VM, Scarfe WC, Bornstein MM. Accuracy of linear measurements on CBCT images related to presurgical implant treatment planning: A systematic review. *Clin Oral Implants Res* 2018;29 Suppl 16:393-415.
  17. Jimenez-Delgado JJ, Paulano-Godino F, PulidoRam-Ramirez R, Jimenez-Perez JR. Computer assisted preoperative planning of bone fracture reduction: Simulation techniques and new trends. *Med Image Anal* 2016;30:30-45.
  18. Bagci U, Udupa JK, Mendhiratta N, Foster B, Xu Z, Yao J, Chen X, Mollura DJ. Joint segmentation of anatomical and functional images: applications in quantification of lesions from PET, PET-CT, MRI-PET, and MRI-PET-CT images. *Med Image Anal* 2013;17:929-45.
  19. Gangwar T, Calder J, Takahashi T, Bechtold JE, Schillinger D. Robust variational segmentation of 3D bone CT data with thin cartilage interfaces. *Med Image Anal* 2018;47:95-110.
  20. Radzi S, Dlaska CE, Cowin G, Robinson M, Pratap J, Schuetz MA, Mishra S, Schmutz B. Can MRI accurately detect pilon articular malreduction? A quantitative comparison between CT and 3T MRI bone models. *Quant Imaging Med Surg* 2016;6:634-47.
  21. Bangerter NK, Taylor MD, Tarbox GJ, Palmer AJ, Park DJ. Quantitative techniques for musculoskeletal MRI at 7 Tesla. *Quant Imaging Med Surg* 2016;6:715-30.
  22. Wang L, Chen KC, Gao Y, Shi F, Liao S, Li G, Shen SG, Yan J, Lee PK, Chow B, Liu NX, Xia JJ, Shen D. Automated bone segmentation from dental CBCT images using patch-based sparse representation and convex optimization. *Med Phys* 2014;41:043503.
  23. Loubele M, Maes F, Jacobs R, van Steenberghe D, White SC, Suetens P. Comparative study of image quality for MSCT and CBCT scanners for dentomaxillofacial radiology applications. *Radiat Prot Dosimetry* 2008;129:222-6.

24. Choi IGG, Cortes ARG, Arita ES, Georgetti MAP. Comparison of conventional imaging techniques and CBCT for periodontal evaluation: A systematic review. *Imaging Sci Dent* 2018;48:79-86.
25. Vandenberghe B, Luchsinger S, Hostens J, Dhoore E, Jacobs R, Consortium SP. The influence of exposure parameters on jawbone model accuracy using cone beam CT and multislice CT. *Dentomaxillofac Radiol* 2012;41:466-74.
26. Carrino JA, Al Muhit A, Zbijewski W, Thawait GK, Stayman JW, Packard N, Senn R, Yang D, Foos DH, Yorkston J, Siewerdsen JH. Dedicated cone-beam CT system for extremity imaging. *Radiology* 2014;270:816-24.
27. Posadzy M, Desimpel J, Vanhoenacker F. Cone beam CT of the musculoskeletal system: clinical applications. *Insights Imaging* 2018;9:35-45.
28. John B, Ludlow MI. Weightbearing CBCT, MDCT, and 2D imaging dosimetry of the foot and ankle. *International Journal of Diagnostic Imaging* 2014;1.
29. Tuominen EK, Kankare J, Koskinen SK, Mattila KT. Weight-bearing CT imaging of the lower extremity. *AJR Am J Roentgenol* 2013;200:146-8.
30. Marzo JM, Kluczynski MA, Clyde C, Anders MJ, Muttu CE, Ritter CA. Weight bearing cone beam CT scan versus gravity stress radiography for analysis of supination external rotation injuries of the ankle. *Quant Imaging Med Surg* 2017;7:678-84.
31. Liang X, Lambrechts I, Sun Y, Denis K, Hassan B, Li L, Pauwels R, Jacobs R. A comparative evaluation of Cone Beam Computed Tomography (CBCT) and Multi-Slice CT (MSCT). Part II: On 3D model accuracy. *Eur J Radiol* 2010;75:270-4.
32. Neubert A, Wilson KJ, Engstrom C, Surowiec RK, Paproki A, Johnson N, Crozier S, Fripp J, Ho CP. Comparison of 3D bone models of the knee joint derived from CT and 3T MR imaging. *Eur J Radiol* 2017;93:178-84.
33. Hovels AM, Heesakkers RA, Adang EM, Jager GJ, Strum S, Hoogeveen YL, Severens JL, Barentsz JO. The diagnostic accuracy of CT and MRI in the staging of pelvic lymph nodes in patients with prostate cancer: a meta-analysis. *Clin Radiol* 2008;63:387-95.
34. Tomiyama N, Honda O, Tsubamoto M, Inoue A, Sumikawa H, Kuriyama K, Kusumoto M, Johkoh T, Nakamura H. Anterior mediastinal tumors: diagnostic accuracy of CT and MRI. *Eur J Radiol* 2009;69:280-8.
35. Rathnayaka K, Momot KI, Noser H, Volp A, Schuetz MA, Sahama T, Schmutz B. Quantification of the accuracy of MRI generated 3D models of long bones compared to CT generated 3D models. *Med Eng Phys* 2012;34:357-63.
36. Van den Broeck J, Vereecke E, Wirix-Speetjens R, Vander Sloten J. Segmentation accuracy of long bones. *Med Eng Phys* 2014;36:949-53.
37. Biedert R, Sigg A, Gal I, Gerber H. 3D representation of the surface topography of normal and dysplastic trochlea using MRI. *Knee* 2011;18:340-6.
38. Suwarganda EK, Diamond LE, Lloyd DG, Besier TF, Zhang J, Killen BA, Savage TN, Saxby DJ. Minimal medical imaging can accurately reconstruct geometric bone models for musculoskeletal models. *PLoS One* 2019;14:e0205628.
39. Wolf P, Luechinger R, Stacoff A, Boesiger P, Stuessi E. Reliability of tarsal bone segmentation and its contribution to MR kinematic analysis methods. *Comput Med Imaging Graph* 2007;31:523-30.
40. Rao C, Fitzpatrick CK, Rullkoetter PJ, Maletsky LP, Kim RH, Laz PJ. A statistical finite element model of the knee accounting for shape and alignment variability. *Med Eng Phys* 2013;35:1450-6.
41. Lee YS, Seon JK, Shin VI, Kim GH, Jeon M. Anatomical evaluation of CT-MRI combined femoral model. *Biomed Eng Online* 2008;7:6.
42. Inoue A, Ohnishi T, Kohno S, Nishida N, Nakamura Y, Ohtsuka Y, Matsumoto S, Ohue S. Usefulness of an Image Fusion Model Using Three-Dimensional CT and MRI with Indocyanine Green Fluorescence Endoscopy as a Multimodal Assistant System in Endoscopic Transsphenoidal Surgery. *Int J Endocrinol* 2015;2015:694273.
43. Al-Saleh MAQ, Alsufyani N, Lai H, Lagravere M, Jaremko JL, Major PW. Usefulness of MRI-CBCT image registration in the evaluation of temporomandibular joint internal derangement by novice examiners. *Oral Surg Oral Med Oral Pathol Oral Radiol* 2017;123:249-56.
44. Leardini A, Belvedere C, Astolfi L, Fantozzi S, Viceconti M, Taddei F, Ensini A, Benedetti MG, Catani F. A new software tool for 3D motion analyses of the musculo-skeletal system. *Clin Biomech (Bristol, Avon)* 2006;21:870-9.
45. Noh H, Nabha W, Cho JH, Hwang HS. Registration accuracy in the integration of laser-scanned dental images into maxillofacial cone-beam computed tomography images. *Am J Orthod Dentofacial Orthop* 2011;140:585-91.
46. Barr C, Bauer JS, Malfair D, Ma B, Henning TD, Steinbach L, Link TM. MR imaging of the ankle at 3 Tesla and 1.5 Tesla: protocol optimization and application to cartilage, ligament and tendon pathology in cadaver specimens. *Eur Radiol* 2007;17:1518-28.

47. Laader A, Beiderwellen K, Kraff O, Maderwald S, Wrede K, Ladd ME, Lauenstein TC, Forsting M, Quick HH, Nassenstein K, Umutlu L. 1.5 versus 3 versus 7 Tesla in abdominal MRI: A comparative study. *PLoS One* 2017;12:e0187528.
48. Siegler S, Konow T, Belvedere C, Ensini A, Kulkarni R, Leardini A. Analysis of surface-to-surface distance mapping during three-dimensional motion at the ankle and subtalar joints. *J Biomech* 2018;76:204-11.
49. McCollough CH, Leng S, Yu L, Fletcher JG. Dual- and Multi-Energy CT: Principles, Technical Approaches, and Clinical Applications. *Radiology* 2015;276:637-53.
50. Johnson TR. Dual-energy CT: general principles. *AJR Am J Roentgenol* 2012;199:S3-8.
51. Grajo JR, Prochowski A, Sahani DV. Dual energy CT in practice: Basic principles and applications. *Applied Radiology* 2016;45:6-12.
52. van Eijnatten M, van Dijk R, Dobbe J, Streekstra G, Koivisto J, Wolff J. CT image segmentation methods for bone used in medical additive manufacturing. *Med Eng Phys* 2018;51:6-16.
53. Matsiushevich K, Belvedere C, Leardini A, Durante S. Quantitative comparison of freeware software for bone mesh from DICOM files. *J Biomech* 2019;84:247-51.
54. Hore S, Chakraborty S, Chatterjee S, Dey N, Ashour AS, Le C, Nhu NG, Le DN. An Integrated Interactive Technique for Image Segmentation using Stack based Seeded Region Growing and Thresholding. *International Journal of Electrical and Computer Engineering* 2016;6:2773-80.
55. Soderkvist I, Wedin PA. Determining the movements of the skeleton using well-configured markers. *J Biomech* 1993;26:1473-7.
56. P.J. Besl NDM. A method for registration of 3-D shapes. *IEEE Trans Pattern Anal Mach Intell* 1992;14:239-56.
57. Dusseldorp JK, Stamatakis HC, Ren Y. Soft tissue coverage on the segmentation accuracy of the 3D surface-rendered model from cone-beam CT. *Clin Oral Investig* 2017;21:921-30.
58. Close J, Inman V. The Action of the Ankle Joint. Prosthetic Devices Research Project, Institute of Engineering Research. University of California (Berkeley) 1952.
59. Inman VT. The joints of the ankle. Baltimore: Williams & Wilkins, 1976.
60. Sancisi N, Baldisserrri B, Parenti-Castelli V, Belvedere C, Leardini A. One-degree-of-freedom spherical model for the passive motion of the human ankle joint. *Med Biol Eng Comput* 2014;52:363-73.
61. Reynier C, Troccaz J, Fourneret P, Dusserre A, Gay-Jeune C, Descotes JL, Bolla M, Giraud JY. MRI/TRUS data fusion for prostate brachytherapy. Preliminary results. *Med Phys* 2004;31:1568-75.
62. Patterh ADaMS. CT and MRI Brain Images Registration for Clinical Applications. *Journal of Cancer Science & Therapy* 2014;6:018-26.
63. Lalone EA, Willing RT, Shannon HL, King GJ, Johnson JA. Accuracy assessment of 3D bone reconstructions using CT: an intro comparison. *Med Eng Phys* 2015;37:729-38.
64. Klintstrom E, Smedby O, Moreno R, Brismar TB. Trabecular bone structure parameters from 3D image processing of clinical multi-slice and cone-beam computed tomography data. *Skeletal Radiol* 2014;43:197-204.
65. Demehri S, Muhit A, Zbijewski W, Stayman JW, Yorkston J, Packard N, Senn R, Yang D, Foos D, Thawait GK, Fayad LM, Chhabra A, Carrino JA, Siewerdsen JH. Assessment of image quality in soft tissue and bone visualization tasks for a dedicated extremity cone-beam CT system. *Eur Radiol* 2015;25:1742-51.
66. Loubele M, Bogaerts R, Van Dijk E, Pauwels R, Vanheusden S, Suetens P, Marchal G, Sanderink G, Jacobs R. Comparison between effective radiation dose of CBCT and MSCT scanners for dentomaxillofacial applications. *Eur J Radiol* 2009;71:461-8.
67. Koivisto J, Kiljunen T, Kadesjo N, Shi XQ, Wolff J. Effective radiation dose of a MSCT, two CBCT and one conventional radiography device in the ankle region. *J Foot Ankle Res* 2015;8:8.
68. Vikhoff-Baaz B, Bergh AC, Starck G, Ekholm S, Wikkelso C. A new set of fiducial markers for MRI, CT and SPET alignment. *Nucl Med Commun* 1997;18:1148-54.
69. You J, Lee YS, Moon Sohn H. Multimodal imaging fiducial markers for kinematic measurement of joint models. *Asian Biomedicine* 2013;7:509-16.
70. Anderson DD, Tochigi Y, Rudert MJ, Vaseenon T, Brown TD, Amendola A. Effect of implantation accuracy on ankle contact mechanics with a metallic focal resurfacing implant. *J Bone Joint Surg Am* 2010;92:1490-500.

**Cite this article as:** Durastanti G, Leardini A, Siegler S, Durante S, Bazzocchi A, Belvedere C. Comparison of cartilage and bone morphological models of the ankle joint derived from different medical imaging technologies. *Quant Imaging Med Surg* 2019;9(8):1368-1382. doi: 10.21037/qims.2019.08.08